AMSE JOURNALS-AMSE IIETA publication-2017-Series: Modelling A; Vol. 90; N°2; pp 142-161
Submitted Mar. 01, 2017; Revised May 13, 2017; Accepted Jun. 13, 2017

Analysis and Design Optimization for Cascade Electromagnetic Transmitter Operating in High Frequency

*Jianzhi Ding, **Yiming Zhang

*Department of Information Technology, Beijing University of Technology, Beijing 100124, China (djzh5@163.com)
**Department of Information Technology, Beijing University of Technology, Beijing 100124, China

Abstract

In the popular electromagnetic exploration technique, a bipolar artificial pulse current is emitted from an electromagnetic transmitter into the ground to generate a transient secondary electromagnetic field in the surface strata, and the geological structure in obtained by analysing the distribution of the secondary magnetic field. This paper presents a cascaded electromagnetic transmitter to overcome the drawbacks of the existing transmitters. First, the structure and composition of the earth load are analysed when the transmitter is working in the low frequency or high frequency mode, and the relationship between the earth load and the emission frequency is provided directly. Then, based on the small-signal model of phase-shifted full-bridge converter, the influencing factors on the stability of the source converter are analysed and summarized in details when the transmitter worked in the whole frequency range. Moreover, we have derived the possible solutions to ensure the steady-state and dynamic features of the source converter output in the whole frequency range. Two methods are developed through detailed analysis: increase the gain of the voltage-loop transfer function, and increase the output filter inductance of the source converter. Finally, the research findings have been verified by a prototype through an experimental simulation.

Key words

Electromagnetic exploration, Cascade, Phase-Shifted Full-Bridge (PSFB), Earth load, Voltage-loop gain, Whole frequency range.

1. Introduction

Electromagnetic exploration is a vital geophysical means to measure the physical properties of the subsurface from the surface of the earth. It is most often used to detect or infer the presence and position of economically useful geological deposits, such as ore minerals, fossil fuels, other hydrocarbons, geothermal reservoirs, and groundwater reservoirs [1]. The centrepiece of electromagnetic exploration is the electromagnetic transmitter. The electromagnetic signal transmitting device converts electrical energy into high-power and variable-frequency square signals of alternating polarity. The signals are emitted to the earth surface to generate transient secondary electromagnetic field in the surface strata. Then, the response signals of the electromagnetic field are received, inverted and processed by receivers for discrimination between stratigraphic or tectonic structures [2].

The exploration accuracy and depth directly hinges on the strength and transient performance of the output electromagnetic field. To achieve deep penetration and high vertical resolution, a viable solution is to install a wide-band sweep-frequency source on the electromagnetic transmitter. The emission frequency of the source, together with the ground conductivity [2-3], determines the depth of penetration. For deeper penetration, more accurate detection and easier field operations, the electromagnetic transmitter must feature light weight, small size, strong anti-interference, high output power, and sound steady-state and transient performance.

In this paper, a cascade electromagnetic transmitter is developed based on the phase-shifted full-bridge (PSFB) structure, aiming to raise the power density and ensure the output power. The PSFB is a popular DC-to-DC topology adopted for high power converters [4-5]. Moreover, the dual closed-loop average current-control strategy was employed in the cascade electromagnetic transmitter to guarantee the output performance [6].

Over the years, much research has been done on cascade converters [7-10]. The researchers mainly focus on analysing and adjusting the stability of cascade converters to maintain the consistency between the output impedance of source converter and the input impedance of load converter [7-9]. For instance, Reference [7] proposes an active damping method which stabilizes the DC microgrids with constant power load by creating a virtual resistance in the front-stage converter. Reference [8] introduces an adaptive active capacitor converter to stabilize the cascade connected converter system. In pursuit of simpler stability evaluation, Reference [9] further transforms the Thevenin/Norton equivalent to feedback the interlinks between cascaded converter

systems of two general classes. Reference [10] discusses the relationship between the self-oscillation of the DC bus and the stability of the cascade connected converter running without load.

In view of the above, this paper presents an electromagnetic transmitter using the cascade architecture. The design and implementation of the transmitter is bound to be affected by the interaction between front-stage and rear-stage. In view of the electromagnetic exploration and the load features of the electromagnetic transmitter, we analysed the influencing factors on the stability of the transmitter working from the low frequency (1Hz) to the high frequency (9,600Hz), and, on this basis, put forward the measure to ensure the stable operation of the transmitter earth load in the course of large range adjustment.

2. Transmitter System

2.1 Structure of the Cascade Electromagnetic Transmitter

According to the system architecture in Fig.1, the cascade electromagnetic transmitter mainly consists of a generator, a three-phase rectifier, a PSFB converter and a launch bridge. The transmitter system operates in the following manner.

First, the three-phase rectifier converts the DC voltage and transmit the converted voltage to the PSFB converter at its output terminal. Then, the PSFB converter, adjustable by a controller, regulates and controls the DC output voltage and output current. Finally, the launch bridge emits artificial current pulses at different frequencies and alternating polarities into the ground.

In particular, the PSBF converter, as the front-stage converter, is responsible for voltage matching and electrical isolation between the launch bridge and power supply. The launch bridge, as the rear-stage converter, completes frequency adjustment of manual current pulse and supplies power to the earth load. Overall, the PSFB converter is the essential circuit to adjust the voltage and current. The transient and steady-state features of the converter directly bear on the performance of electromagnetic transmitter system.

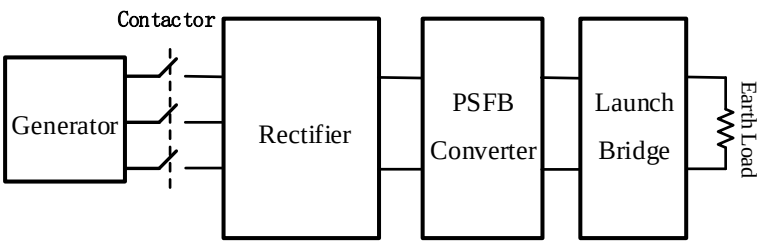

Fig.1. System Architecture of the Cascade Electromagnetic Transmitter

2.1 Structure and Composition of Earth Load

The principle and operation electromagnetic exploration requires that the current pulses of alternating polarity must be emitted at adjustable frequencies. The frequency of the launch bridge ranges from 1Hz to 9,600Hz [11]. When the launch bridge emits current pulses at a low frequency, the equivalent earth load is considered as a pure resistive load (Fig.2a); when the launch bridge emits current pulses at a high frequency, the equivalent earth load is deemed as a composite load made up of resistors, capacitors and inductors (Fig.2b) [12-13].

There is a marked difference between the high-frequency load and low-frequency load of the electromagnetic transmitter. In low-frequency operations, the equivalent earth load is rather small. In high-frequency operations, however, the equivalent earth load reduces with the increase in emission frequency, and even the source converter runs under a light load.

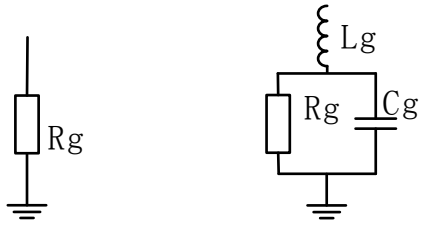

(a) (b)

Fig.2. Equivalent Earth Load Circuit

The equivalent earth load of the transmitter at a low frequency and a high frequency can be calculated by formulas (1) and (2), respectively.

$$Z_{low\_Ld}(s) = R_g \tag{1}$$

$$Z_{high\_Ld}(s) = 2\pi fL_g + R_g \Big/ \left(2\pi fC_g R_g + 1\right) \tag{2}$$

With such a wide range of load, it is necessary to analyse the relationship between the actual load variation and the dual-loop compensation parameters of the source converter. In addition, the values of the equivalent earth load (e.g. R_g, C_g and L_g) should be altered according to the soil salinity, water saturation and geological structure. For the design and analysis of the transmitter,

the earth load was taken from a certain place in western China for calculation. The specific data are shown in Table 1.

3. Small-signal Modelling

Featuring simple, reliable control, good efficiency and high power density, the zero-voltage switching (ZVS) PSFB converter topology was adopted to achieve the zero-voltage operation of the switch tube on the launch bridge. The ZVS-PSFB utilizes the leakage inductance of the isolation transformer, together with the source-drain parasitic capacitance resonance of the switch tube [14-15].

Fig. 3 illustrates the small-signal modelling of the source converter. Under the combined effect of the phase-shift operation and the leakage inductance L_k of the transformer, the secondary side of the transformer may suffer from the "loss of duty-cycle" [15]. The voltage effective duty-cycle on the secondary side is expressed as follows.

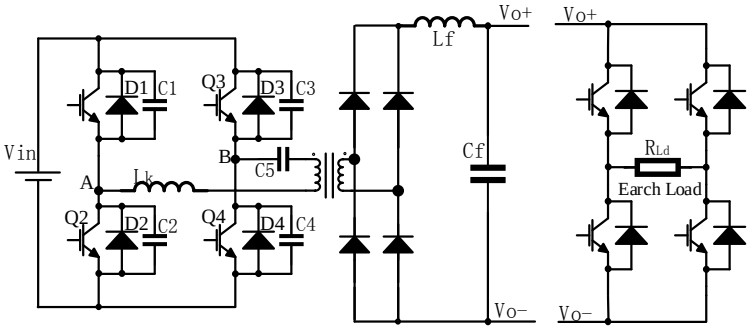

(a) (b)

Fig.3. Key Modules of Electromagnetic Transmitter

(a) Source Converter; (b) Launch Bridge

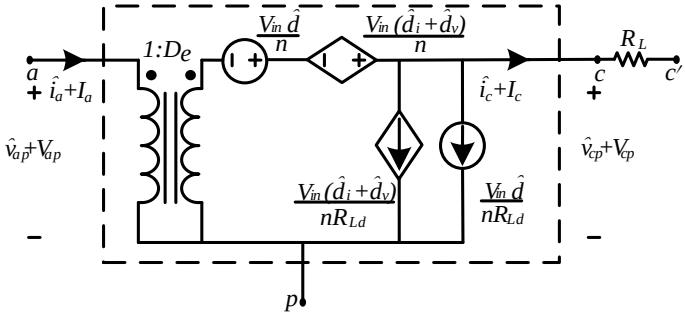

Fig.4. Circuit Model of the PWM Switch for the Electromagnetic Transmitter

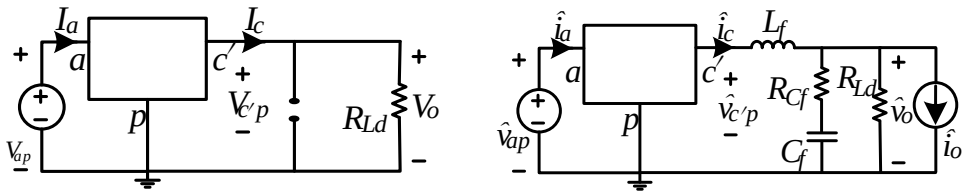

Fig.5. (a) Equivalent DC Model; (b) Equivalent Small-signal Model

$$D_e = D - \frac{2 f_s L_k}{n V_{in}} (2 I_L - \frac{V_o D'}{2 f_s L_f}) \tag{3}$$

where D is the duty-cycle of the primary voltage configured by the controller; f_s is the switching frequency; L_k is the leakage inductance of the transformer; $n=n_p/n_s$ is the turns ratio of the transformer; I_L is the output inductor current; L_f is the output inductance; V_{in} is the input voltage; V_o is the output voltage; $D'=1-D$.

Considering the duty-cycle modulation resulted from variation in the current of the output filter inductor $\hat{d}_i$ and the input voltage $\hat{d}_v$, the total variation in the effective-duty $\hat{d}_e$ can be expressed as:

$$\hat{d}_e = \hat{d} - \hat{d}_i - \hat{d}_v \tag{4}$$

Figure 4 displays the corresponding circuit model of the PWM switch for the electromagnetic transmitter. The letters *a, p* and *c'* stand for the equivalent functional blocks of the three terminals, including the PWM switch blocks, denoted as *a*, *p* and *c*, and the equivalent series resistance (ESR) R_L of the filter inductance (between terminals *c* and *c'*).

The equivalent models of the source converter are shown in Figures 5(a) and 5(b), respectively. Considering the equivalent DC model of the source converter, the resulting circuit equations are as follows:

$$I_a = D_e I_c \tag{5}$$

$$V_{cp} = D_e V_{ap} \tag{6}$$

$$V_{cp} = R_L I_c + V_{c'p} \tag{7}$$

where $V_{ap}=V_{in}/n$ and $V_{c'p}=V_o$.

As for the equivalent small-signal model, the resulting circuit equations are as follows:

$$\hat{i}_a = D_e \hat{i}_c + \hat{d}_e I_c \tag{8}$$

$$\hat{i}_c = \hat{i}_{Cf} + \hat{v}_o / R_{Ld} + \hat{i}_o \tag{9}$$

$$\hat{v}_{cp} = D_e \hat{v}_{ap} + \hat{d}_e V_{ap} \tag{10}$$

$$\hat{v}_{cp} = \left(R_L + sL_f \right) \hat{i}_c + \hat{v}_{c'p} \tag{11}$$

$$\hat{v}_o = \left(R_{Cf} + 1/sC_f \right) \hat{i}_{Cf} \tag{12}$$

$$\hat{d}_e = \hat{d} - \frac{R_d}{V_{ap}} \hat{i}_c + \left(I_c - \frac{V_o D'_e}{4 f_s L_f} \right) \frac{R_d}{V_{ap}^2} \hat{v}_{ap} \tag{13}$$

where $\hat{v}_{ap}= \hat{v}_{in}/n$, $\hat{v}_{c'p}= \hat{v}_o$, $R_d=4f_sL_k/n^2$ and $D'_e=1-D_e$.

According to formulas (8-13), the following are the transfer functions related to the source converter working in the CCM model.

$$Z_f(s) = \frac{1}{H_e(s)} \frac{R_{Ld}\left(sC_f R_C + 1 \right)}{sC_f \left(R_C + R_{Ld} \right) + 1} \tag{14}$$

$$H_e(s) = \frac{R_{Ld}\left(sC_f R_C + 1 \right)}{\left(sL_f + R_L \right)\left[sC_f \left(R_C + R_{Ld} \right) + 1 \right] + R_{Ld}\left(sC_f R_C + 1 \right)} \tag{15}$$

$$G_{v_O d}(s) = \frac{V_{in}}{n} \frac{H_e(s) Z_f(s)}{Z_f(s) + R_d} \tag{16}$$

$$G_{i_L d}(s) = \frac{V_{in}/n}{Z_f(s) + R_d} \tag{17}$$

where $Z_f(s)$ is the transfer function of the output filter; $H_e(s)$ is the input impedance of the output filter.

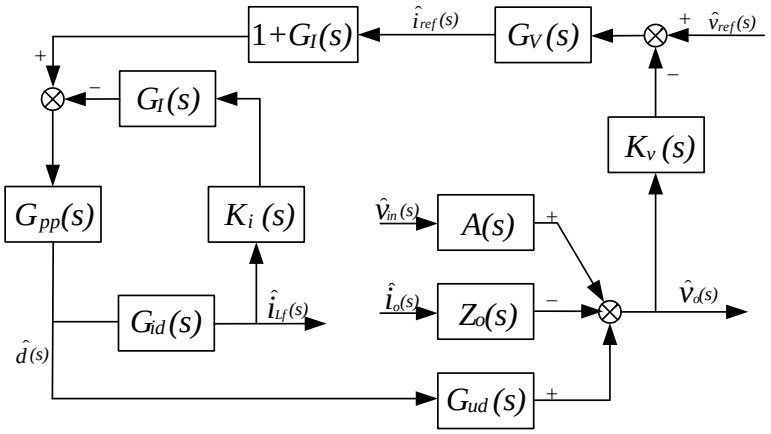

Fig.6. Average-current Control Block Diagram

In light of the Figure 6, it is possible to deduce the following functions.

$$T_{oi}(s) = G_{pp}(s) G_{id}(s) K_i(s) \tag{18}$$

$$T_i(s) = G_I(s) G_{pp}(s) G_{id}(s) K_i(s) \tag{19}$$

$$T_{ov1}(s) = \frac{K_v(s) G_{pp}(s) G_{v_O d1}(s)\left(G_I(s)+1\right)}{T_i(s)+1} \tag{20}$$

$$T_{v1}(s) = \frac{K_v(s) G_V(s) G_{pp}(s) G_{v_O d1}(s)\left(G_I(s)+1\right)}{T_i(s)+1} \tag{21}$$

where $T_{oi}(s)$ is the transfer function of the uncompensated current-loop; $T_i(s)$ is the transfer function of the compensated current-loop; $T_{ov}(s)$ is the transfer function of the uncompensated voltage-loop; $T_o(s)$ is the transfer function of the compensated voltage-loop; $K_i(s)$ is the transfer function of the current sampling coefficient; $K_v(s)$ is the transfer function of the voltage sampling coefficient; $G_{pp}(s)$ is the transfer function of the PWM operations; $G_{pp}(s)=1/V_{pp}$; $G_I(s)$ and $G_V(s)$ are the transfer functions of the current-loop and voltage-loop compensation network, respectively.

The control-loop of the source converter operates similarly in the DCM mode and the CCM mode. However, the transfer function of the duty-cycle to output-voltage differs from that in the CCM [15]:

$$G_{v_{O}d2}(s)=\frac{2(1-M)}{M(2-M)}\sqrt{\frac{1-M}{K}}\frac{V_o}{s\frac{2(1-M)R_{Ld}C_f}{2-M}+1} \tag{22}$$

where $K = 2L_f / (R_{Ld} * T_S)$, and $M = D_1 / (D_1+D_2)$.

When the converter works in the DCM mode, D_1 is the rise time of the output inductor current in a duty-cycle, and D_2 is the fall time of the output inductor current in a duty-cycle.

If the launch bridge is operating at high frequencies, the source converter will shift from the CCM mode to the DCM mode due to the rapid reduction of the earth load. According to formulas (21) and (22), the open-loop transfer function of the compensated voltage-loop is deduced as follow:

$$T_{v2}(s)=\frac{K_v(s)G_V(s)G_{pp}(s)G_{v_{O}d2}(s)(G_I(s)+1)}{T_i(s)+1} \tag{23}$$

Stability, dynamicity and immunity are the three key indicators of the performance of the electromagnetic transmitter. The stability is mainly reflected by the phase margin (>45°) and magnitude margin (>6dB). The dynamicity is often measured by the open-loop cross-over frequency. The greater the cross-over frequency, the faster the dynamic response. The cross-over frequency is limited by the switching frequency of the source converter. The purpose is to eliminate high frequency disturbances caused by the switch.

For the source converter with average current-control, the cross-over frequency of the inner current-loop should be different from that of the outer voltage-loop, so as to prevent the weak dynamic features of the interaction between the two closely arranged loops. Hence, the cross-over frequency of the current loop is generally 30 times greater than that of the voltage-loop.

The single-pole and single-zero compensation network was adopted to design the voltage-loop and current-loop, respectively.

$$G_V(s)=K_{GV}\frac{s/\omega_{ZV}+1}{s/\omega_{ZV}(s/\omega_{PV}+1)} \tag{24}$$

$$G_I(s)=K_{GI}\frac{s/\omega_{ZI}+1}{s/\omega_{ZI}(s/\omega_{PI}+1)} \tag{25}$$

4. Simulation and Analysis

The specific parameters of the proposed cascade electromagnetic transmitter are listed in Table 1. The dual-loop control parameters of the source converter were calculated by formulas (24-25) (Table 2).

Tab.1. Parameters of the Electromagnetic Transmitter

Parameter	Value	Parameter	Value
V_{in}	530 V	L_f	20 μH
V_o	750 V	R_L	0.4 mΩ
I_o	20 A	C_f	400 μF
n	1 : 2.25	R_{Cf}	9.4 mΩ
L_k	0.94 μH	R_g	40 Ω
f_s	20 kHz	C_g	1 nF
$K_i(s)$	0. 1	L_g	0.1 mH
$K_v(s)$	0.005	V_{pp}	2.35 V

According to the design principles of the compensation transfer function, the current close-loop transfer function $T_i(s)$ and the voltage close-loop transfer function $T_v(s)$ were designed for compensation in the CCM mode (Figure 7). The current-loop transfer function increases a pole to elevate the low-frequency gain of the source converter, thereby enhancing the stability and accuracy of the proposed transmitter.

Tab.2. Control Parameters of the Dual-loop

Current-loop		Voltage-loop	
K_{GI}	7.8×10^{-4}	K_{GV}	6.1×10^{-4}
ω_{ZI}	8.7×10^{4}	ω_{ZV}	3.21×10^{4}
ω_{PI}	1.72×10^{6}	ω_{PV}	1.25×10^{5}

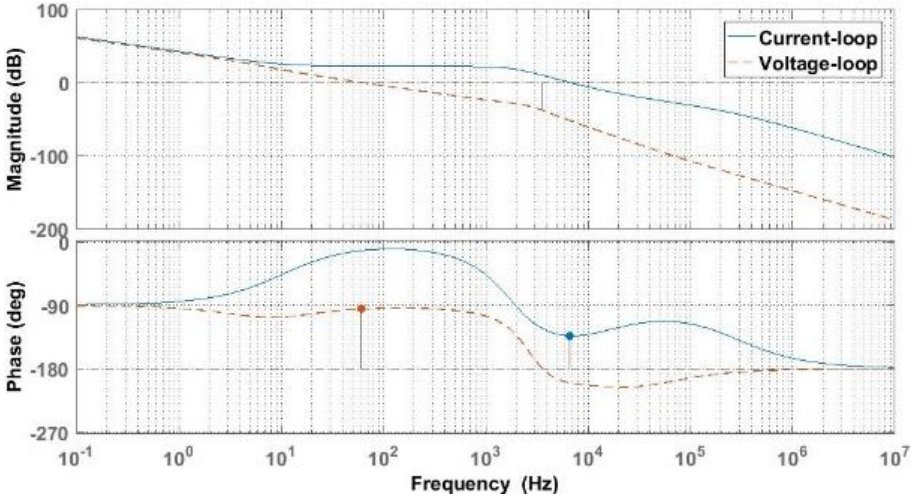

Fig.7. Bode Plot of the Two Loops Compensated in the CCM

In Figure 7, the cross-over frequency of $T_i(s)$ was 6.62 kHz, lower than the switching frequency of 20 kHz, and the phase margin of the function was 47°, wider than the normal standard of 45°. For the $T_v(s)$, the cross-over frequency and the phase margin were 61 Hz and 85°, respectively. Hence, the cross-over frequency of the current-loop was more than 109 times that of the voltage-loop, which had effectively avoided the interaction between the two loops.

Next, the voltage-loop Nyquist curve of the source converter in the DCM mode has been drawn when the electromagnetic transmitter emits current pulses at a high frequency (Figure 8). According to the Nyquist stability criterion, the necessary and sufficient condition for the stability of the closed-loop control system lies in that the number of turns of the Nyquist curve should not exceed (-1, j0) and equal the number of positive real poles in the voltage-loop transfer function.

As shown in Fig.8, there is no turn of the Nyquist curve, and the poles are calculated as -1.72×10^6, -1.25×10^5, -8847-14284i, -8847 + 14284i, -73, -11 and 0; none of the poles is located in the right half of the plane. Since the results could satisfy the Nyquist stability criterion, the compensated system was stable in the DCM mode.

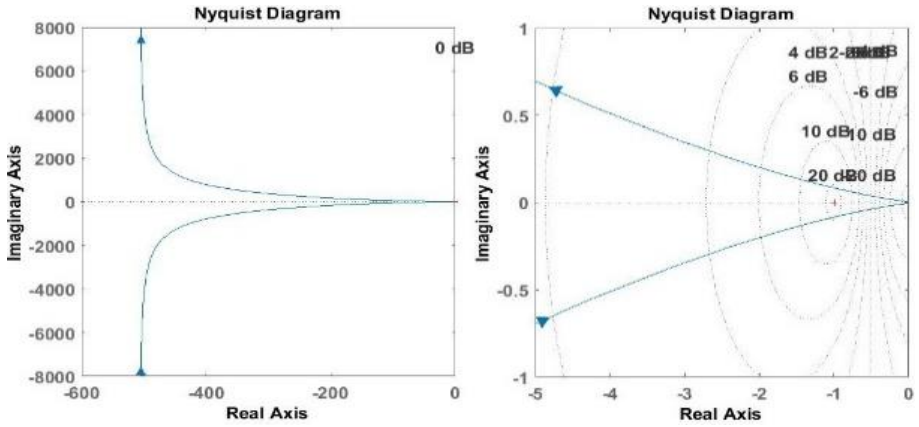

Fig.8. Nyquist Curve of Voltage-loop

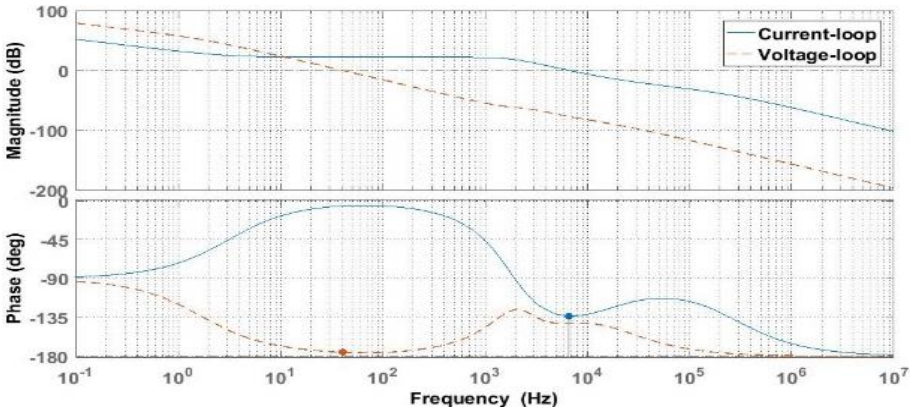

Fig.9. Bode Plot of the Dual-loop Compensated in the DCM

Figure 9 presents the Bode plot of the dual-loop transfer function in the DCM mode. As can be seen from the figure, the cross-over frequencies of $T_i(s)$ and function $T_v(s)$ were 6.62 kHz and 40 Hz, respectively, and the phase margin of $T_i(s)$ and function $T_v(s)$ were 47°and 5°, respectively. The results indicate that the system was also stable in the DCM mode at high frequencies. However, the phase margin corresponding to the cross-over frequency of the voltage close-loop compensator approximated -180°. The extremely small phase margin may pose some risks to the stability of the voltage control-loop of the source converter.

To improve the stability of the cascade electromagnetic transmitter in high frequency mode, the influencing factors were analyzed and measured to enhance the stability of the source converter in the whole emission frequency range.

Figure 10 is the Bode plot of voltage-loop transfer function at different R_g for the transmitter in high frequency mode. With the increase of the resistance component of the earth load, both the phase margin and the cross-over frequency of the voltage closed-loop transfer function $T_v(s)$ of the source converter decreased. When the resistance component increased to 75 Ω or more, the phase margin turned negative, indicating that the converter entered an unstable state.

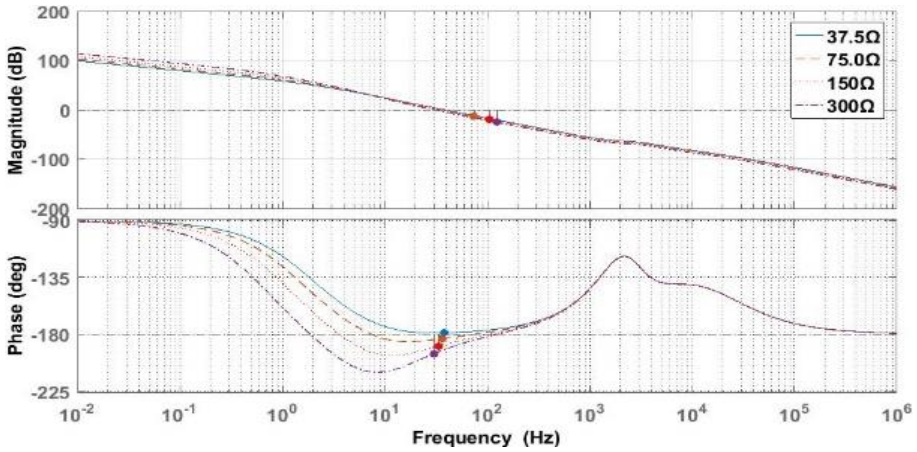

Fig.10. Bode Plot of $T_v(s)$ at Different R_g for the Transmitter in High Frequency Mode

Figure 11 is the Bode plot of voltage-loop transfer function at different C_g for the transmitter in high frequency mode. As shown in the figure, both the phase margin and cross-over frequency increased with the capacitance component of the earth load. In other words, the stability of the voltage close-loop was positively correlated with the capacitance component of the earth load.

Figure 12 is the Bode plot of voltage-loop transfer function at different L_g for the transmitter in high frequency mode. It can be seen that both the phase margin and the cross-over frequency of $T_v(s)$ dropped with the increase in the inductance component of the earth load. When the inductance component rose to 2mH or more, the phase margin became negative, marking the start of the unstable state of the voltage close-loop of the source converter.

Figure 13 is the Bode plot of voltage-loop transfer function at different emission frequencies for the transmitter in high frequency mode. As the emission frequency grew, both the phase margin and the cross-over frequency of $T_v(s)$ exhibited a trend of decline. When the emission frequency reached 9,600 Hz, the phase margin approximated zero. This means the voltage close-loop of the source converter faced a certain risk of instability.

Figure 14 is the Bode plot of voltage-loop transfer function at different output filter capacitances for the transmitter in high frequency mode. As shown in the figure, the elevation of output filter capacitance had no irresistible effect on improving the source converter stability. With the increase of the output filter capacitance, both the phase margin and cross-over frequency of the $T_v(s)$ plummeted. When the output filter capacitance climbed up to 800 μF, the phase margin turned negative, which signifies the instability of the voltage close-loop of the source converter. It must be noted that the ripple voltage of the output DC bus may grow at the decline of the output capacitance, making it necessary to strike a balance between the ripple voltage of the output DC bus and the source converter stability.

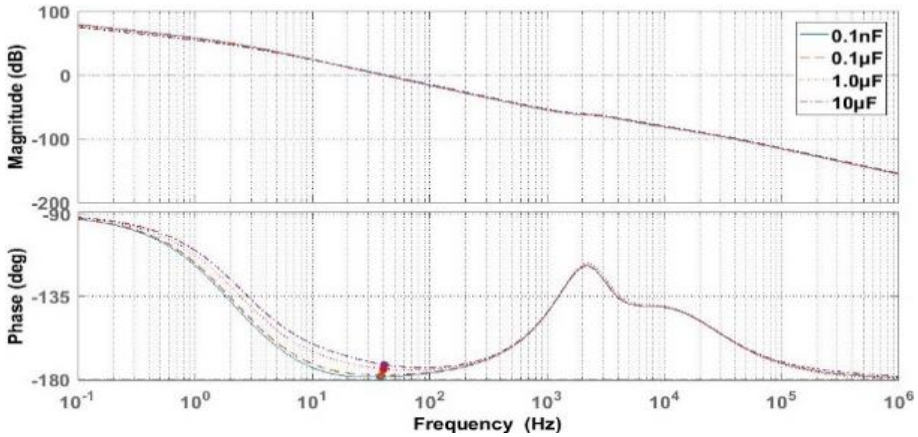

Fig.11. Bode Plot of $T_v(s)$ at Different C_g for the Transmitter in High Frequency Mode

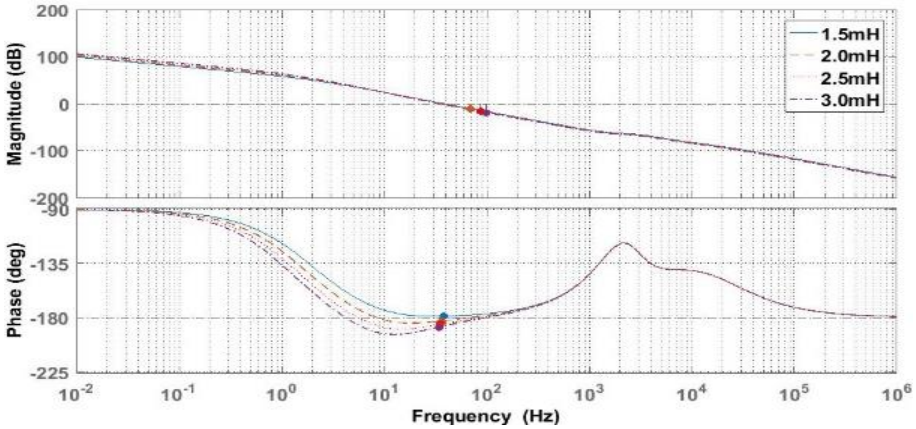

Fig.12. Bode Plot of $T_v(s)$ at Different L_g for the Transmitter in High Frequency Mode

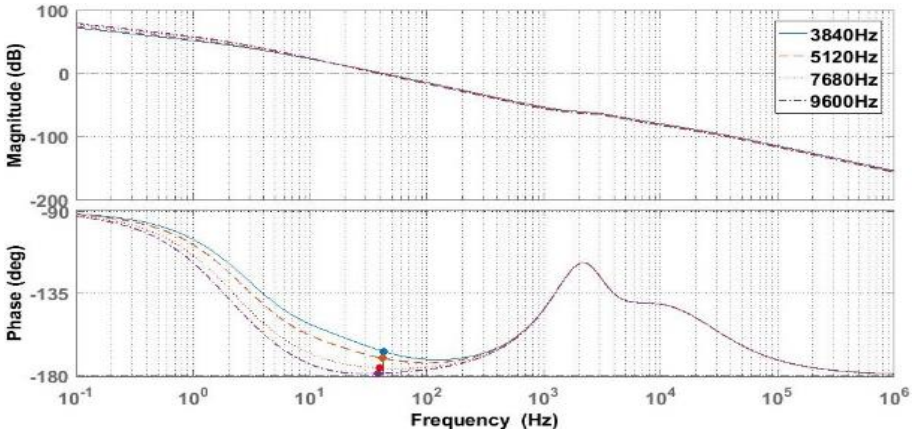

Fig.13. Bode Plot of $T_v(s)$ at Different Emission Frequencies for the Transmitter in High Frequency Mode

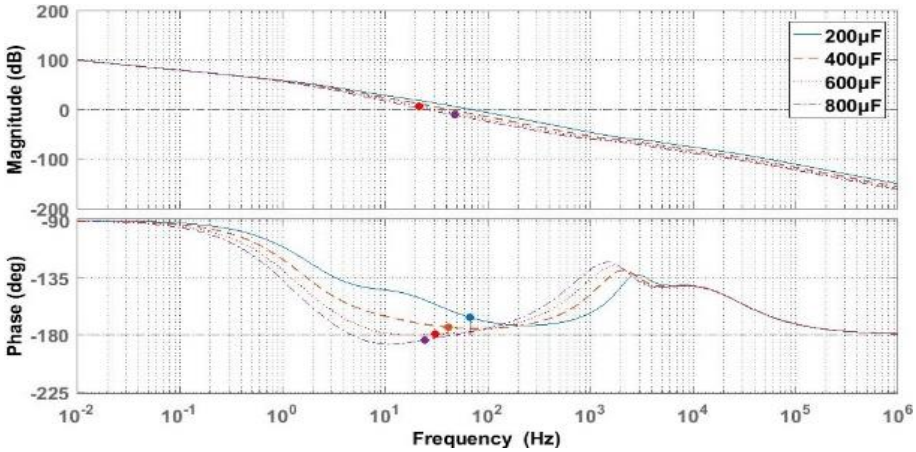

Fig.14. Bode Plot of $T_v(s)$ At Different Output Filter Capacitances for the Transmitter in High Frequency Mode

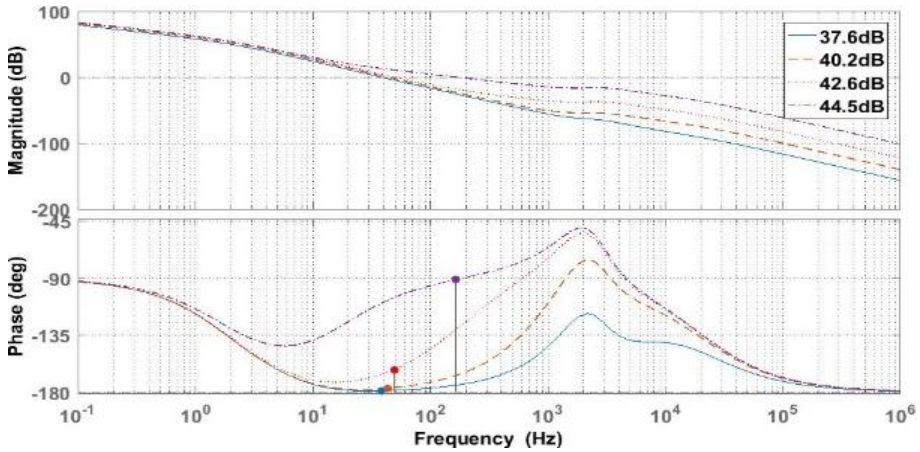

Fig.15. Bode Plot of $T_V(s)$ at Different Voltage-loop Gains for the Transmitter in High Frequency Mode

Figure 15 is the Bode plot of voltage-loop transfer function at different voltage-loop gains for the transmitter in high frequency mode. According to the figure, the voltage closed-loop gain stood at 1 Hz. The gain was increased by shifting the zero of the voltage-loop transfer function to the right and increasing the proportion coefficient of the transfer function GV(s). The gain enhancement method had suppressed the decline in stability of the source converter. With the increase in the phase margin of the transfer function, the voltage loop of the corresponding source converter achieved better stability. When ωZV = 90.21 and KGV = 0.7, the phase margin of the voltage-loop reached 89°, which is greater than 45°. With the increase in the phase margin of the voltage-loop, however, the cross-over frequency of the voltage-loop approximated that of the current-loop, exerting a negative effect on the control of the dual-loop.

Through the previous analysis, it is concluded that the output voltage stability of the cascade electromagnetic transmitter in high frequency mode depends on many factors. Among them, the multiple components (e.g. Rg, Cg and Lg) and emission frequency cannot be adjusted to improve the stability of the transmitter, because they are either inherent features of the earth load or the conditions of the electromagnetic exploration. Therefore, the only way to enhance the transmitter stability lies in reducing the output filter capacitance and increasing the voltage-loop gain of the source converter.When the transmitter works at a high frequency, its stability can be improved by lowering the output filter capacitance. However, if it runs at a low frequency, the output ripple voltage may decline. The voltage-loop gain can be expanded by moving the zero of the transfer function $G_V(s)$ to the right and increasing the proportion coefficient of $G_V(s)$. With the increase in the voltage-loop gain, it is easy and effective to maintain the stability of the cascaded

electromagnetic transmitter across the whole frequency range, minimize the transmitter weight and increase power density.

It should be noted that an increase in the output inductance of the source converter also helps to maintain the stable operation of the source converter in the CCM mode, and achieve the stable output of the transmitter across the whole frequency range. Of course, such a method will greatly increase the weight of the transmitter.

5. Experimental Results

A prototype of the cascade electromagnetic transmitter (Figure 1) was built to verify the results of the previous analysis.

Fig.16 and Fig.17 present the waveforms of emission voltage and current of the transmitter in low frequency mode and high frequency mode, respectively. As shown in Figure 16, the emission voltage was 750 V and the emission current was 19 A when the transmitter ran at a low frequency. As shown in Figure 17, the emission voltage was 750 V and the peak emission current was 6 A when the transmitter ran at a high frequency.

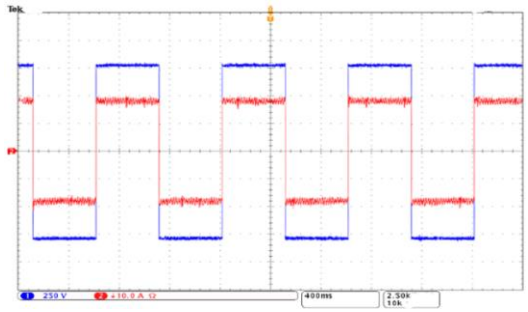

Fig.16. Emission Voltage and Emission Current Waveforms of the Transmitter at 1 Hz

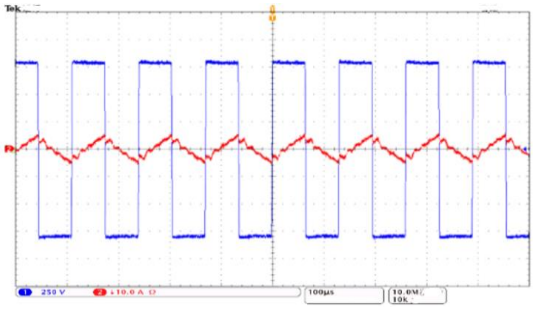

Fig.17. Emission Voltage and Emission Current Waveforms of the Transmitter at 9,600 Hz

Figure 18 and Figure 19 display the output DC voltage waveforms of the source converter in the DCM when the output filter has a capacitance of 400 μF or 1,000 μF, respectively. When the

transmitter operated at a high frequency, the DC output stability was very poor at the output filter capacitance of 1,000 μF, with the DC voltage peaking at 130 V; the DC output stability was significantly improved at the output filter capacitance of 400 μF, with the DC voltage peaking at 20 V.

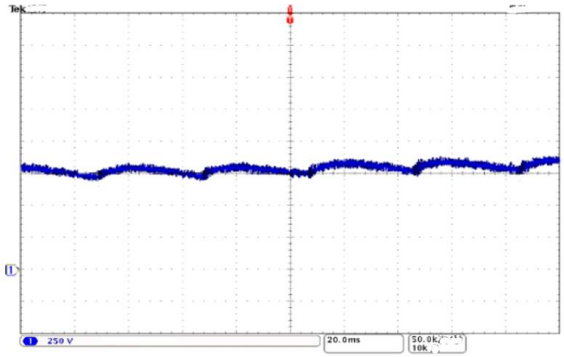

Fig.18. Output DC voltage waveform of the source converter at the output filter capacitance of 1,000 μF

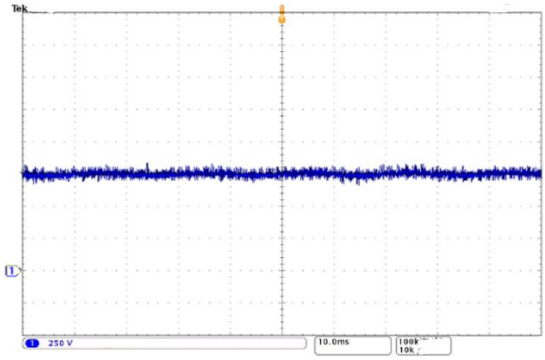

Fig.19. Output DC Voltage Waveform of Source Converter at the Output Filter Capacitance of 400 μF

Figure 20 and Figure 21 exhibit the emission voltage waveforms of the transmitter in high frequency mode at the voltage-loop gain of 37.6 dB or 44.5 dB, respectively. It can be seen that the transmitter had obvious emission voltage waveform oscillation at the voltage-loop gain of 37.6 dB, while the emission voltage waveform is flat at the voltage-loop gain of 44.5 dB, indicating excellent output performance of the transmitter.

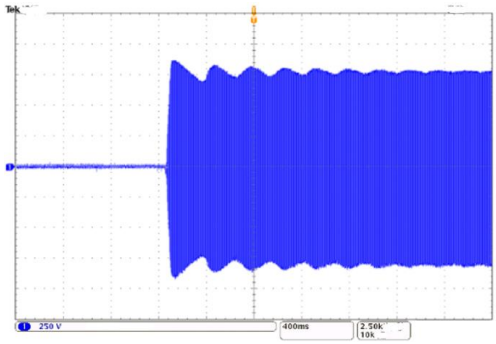

Fig.20. Emission Voltage Waveform of the Transmitter in High Frequency Mode at the Voltage-Loop Gain of 37.6 dB

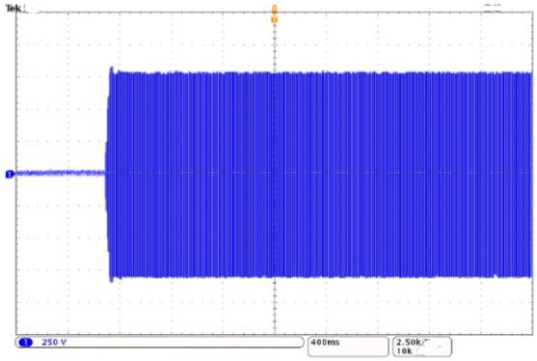

Fig.21. Emission Voltage Waveform of the Transmitter in High Frequency Mode at the Voltage-Loop Gain of 44.5 dB

Conclusion

This paper presents a cascaded electromagnetic transmitter to overcome the drawbacks of the existing transmitters. First, the structure and composition of the earth load were analysed when the transmitter is working in the low frequency or high frequency mode, and the relationship between the earth load and the emission frequency was provided directly. Then, the influencing factors on the stability of the source converter in high frequency mode were analysed and summarized based on the small-signal model of the source converter working in the CCM or the DCM. Moreover, we looked for the possible solutions to ensure the steady-state and dynamic features of the source converter output in two operation modes. The voltage-loop gain enhancement was pointed out as a scientific and positive way to guarantee the steady-state and dynamic features of the source converter when the transmitter ran in high-frequency mode. Finally, the proposed method was verified by a prototype through an experimental simulation.

References

1. T.C. Sun, Z.H. Fu, H.M. Tai, Q.L. Chen, Application of ramp turn-off transient electromagnetic method in shallow exploration, 2008, World Automation Congress, Hawaii, USA, pp. 1-4.
2. Y.A. Manstein, A.K. Manstein, E. Balkov, G. Panin, A. Scozzari, Non-invasive measurements for shallow depth soil exploration: Development and application of an electromagnetic induction instrument, 2015, IEEE International Instrumentation and Measurement Technology Conference (I2MTC) Proceedings, Pisa, Italy, pp. 1395-1399.
3. A. Ansari, A.B. Shafie, S. Ansari, A.B.M. Said, E.T. Nyamasvisva, M. Abdulkarim, M. Rauf, Subsurface exploration of seabed using electromagnetic waves for the detection of hydrocarbon layers, 2014, International Conference on Computer and Information Sciences (ICCOINS), Kuala Lumpur, Malaysia, pp. 1-5.
4. M. Agamy, D. Dong, L. Garces, Y. Zhang, M.E. Dame, X. Wu, Y. Pan, A high power medium voltage resonant dual active bridge for MVDC ship power networks, 2016, IEEE Journal of Emerging and Selected Topics in Power Electronics, vol. 5, no.1, pp. 88-99.
5. D.S. Gautam, F. Musavi, W. Eberle, W.G. Dunford, A Zero-Voltage switching Full-Bridge DC-DC converter with capacitive output filter for Plug-In Hybrid Electric Vehicle Battery Charging, 2013, IEEE Transactions on Power Electronics, vol. 28, no. 12, pp. 5728-5735.
6. X. Zhang, C. Li, H. Yang, Y. Guan, Control strategy analysis and loop design of full-bridge phase-shift soft-switching DC-DC converter, 2016, IEEE 8th International Power Electronics and Motion Control Conference (IPEMC-ECCE Asia), Hefei, China, pp. 1139-1145.
7. M.F. Wu, D.D.C. Lu, Adding virtual resistance in source side converters for stabilization of cascaded connected two stage converter systems with constant power loads in DC microgrids, 2014, International Power Electronics Conference, Hiroshima, Japan, pp. 3553-3556.
8. X. Zhang, X. Ruan, H. Kim, C.K. Tse, Adaptive active capacitor converter for improving stability of cascaded DC power supply system, 2013, IEEE Transactions on Power Electronics, vol. 28, no. 4, pp. 1807-1816.
9. S. Liu, X. Liu, Y.F. Liu, Analysis on feedback interconnections of cascaded DC-DC converter systems, 2015, IEEE Energy Conversion Congress and Exposition (ECCE), 2015, Montreal, Canada, pp. 5160-5166.
10. Y.H. Chen., W. Zhen, J.W. Chen, C.Y. Gong, DC bus self-oscillation suppression and optimal design for cascade aviation static inverter, 2013, 8th IEEE Conference on Industrial Electronics and Applications (ICIEA), pp. 1095-1100.

11. Z.G. An, Q.Y. Di, C.M. Fu, C. Xu, B. Cheng, Geophysical evidence through a CSAMT survey of the deep geological structure at a potential radioactive waste site at Beishan, Gansu, China, 2013, Journal of Environmental and Engineering Geophysics. vol. 18, no.1, pp. 43-54.
12. S. Shozo, Discussion of current dependent grounding resistance using an equivalent circuit considering frequency-dependent soil parameters, 2016, 33rd International Conference on Lightning Protection (ICLP), Estoril, Portugal, pp. 1-6.
13. G. Leonid, P. Marjan, On high-frequency circuit equivalents of a vertical ground rod, 2005, IEEE Transactions on power delivery, vol. 20, no. 2, pp. 1598-1603.
14. G.D. Capua, S.A. Shirsavar, M.A. Hallworth, An Enhanced Model for Small-Signal Analysis of the Phase-Shifted Full-Bridge Converter, 2015, IEEE Transactions on Power Electronics. vol. 30, no. 3, pp. 1567-1576.
15. T. Mishima, K. Akamatsu, M. Nakaoka, A high frequency-link secondary-side phase-shifted full-range soft-switching PWM DC-DC converter with ZCS active rectifier for EV battery chargers, 2013, IEEE Transactions on Power Electronics, vol. 28, no. 12, pp. 5758-5773.
16. J. Cho, J. Baek, Y.J. Chang, G. Rim, Novel zero-voltage and zero-current-switching fullbridge PWM converter using a simple auxiliary circuit, 1999, IEEE Transactions on Industry Applications, vol. 35, no.1, pp. 15-20,